Texture-based Intraoperative Image Guidance for Tumor Localization in Minimally Invasive Surgery*

Arefin Shamsil, Michael D. Naish, *Member, IEEE*, and Rajni V. Patel, *Life Fellow, IEEE*

Abstract— Intraoperative tumor localization in a deflated lung in minimally invasive surgery (MIS) is challenging as the lung cannot be manually palpated through small incisions. To do so remotely, an articulated multisensory imaging device combining tactile and ultrasound sensors was developed. It visualizes the surface tactile map and the depth of the tissue. However, with little maneuverability in MIS, localizing tumors using instrumented palpation is both tedious and inefficient. In this paper, a texture-based image guidance system that classifies tactile-guided ultrasound texture regions and provides beliefs on their types is proposed. The resulting interactive feedback allows directed palpation in MIS. A *k*-means classifier is used to first cluster gray-level co-occurrence matrix (GLCM)-based texture features of the ultrasound regions, followed by hidden Markov model-based belief propagation to establish confidence about the clustered features observing repeated patterns. When the beliefs converge, the system autonomously detects tumor and nontumor textures. The approach was tested on 20 *ex vivo* soft tissue specimens in a staged MIS. The results showed that with guidance, tumors in MIS could be localized with 98% accuracy, 99% sensitivity, and 97% specificity.

Clinical Relevance— Texture-based image guidance adds efficiency and control to instrumented palpation in MIS. It renders fluidity and accuracy in image acquisition using a hand-held device where fatigue from prolonged handling affects imaging quality.

I. INTRODUCTION

Thoracotomy-based surgical resection of early stage lung tumors can treat lung cancer but causes trauma and pain and requires longer recovery time [1]. MIS can mitigate these effects but needs intraoperative tumor localization. Although preoperative CT shows tumor size, shape, and location in the lung, deflating the lung for surgery changes all of these parameters. Intraoperative imaging can provide visualization in MIS to enable examination of target sites and delivery of high-precision treatment [2]. Ultrasound (US) imaging is a real-time modality that can be combined with other modalities for accurate guidance and safer navigation [3]. However, it may not work well on a deflated lung when it contains residual air [4]. Tactile imaging is another real-time modality that uses tactile feedback to detect occult tumors [5]. We anticipate that by fusing tactile and US imaging, tumors in a deflated lung can be adequately localized in MIS.

Prior work involved combining tactile and US sensors in mechatronic and robotic instruments [6, 7] to enable articulated tissue palpation to acquire multimodal images [8]. Experiments showed that finding tumors in *ex vivo* specimens in MIS required concurrent visualization of the intraoperative image and the phantom thoracic cavity [8, 9]. The imaging procedure included instrument-assisted palpation and image interpretation while cognitively tracking the palpated sites. These were labor- and memory-intensive tasks that, combined with limited instrument maneuverability in MIS, made tumor localization very inefficient. To address this issue, automated image interpretation was considered. Texture characterization is a method to detect heterogeneous regions in images [10]. Texture analysis to identify solid, semi-solid, and nonsolid lung tumors has been an active area of research [11]. A study on endobronchial US imaging showed that texture features for benign and malignant tumors are statistically different [12]. Linear classifiers can differentiate textures of lung diseases on US images [13], but their viability in sequential US imaging is not yet known. However, hidden Markov models (HMMs) have shown success in characterizing tumor by capturing differing temporal signatures in sequential US imaging [14].

In this paper, a method for texture-based image guidance to efficiently localize tumors in *ex vivo* specimens in staged MIS experiments is presented. It adopts an artificial intelligence (AI) approach that uses a *k*-means classifier [15] to cluster gray-level co-occurrence matrix (GLCM) texture features [16] of the tactile-guided US regions. It then uses an HMM to gradually learn the feature characteristics from patterns accumulated in the clusters over time. Finally, it applies Bayes' filtering [17] to the tactile–US feeds to estimate beliefs about the texture types defined by the feature clusters. Interactive visualization of these beliefs may be used to direct tissue palpation to capture similar textures in the tactile–US images acquired. These additional images further improve the beliefs and the subsequent image guidance. To conclude, palpation results using texture-based image guidance are compared with palpation results without texture-based image guidance, and with other published work.

II. METHOD

A. Previous Work

A knowledge-encoded feature detector (**K*e*FD**) was developed. It detects tactile spots in a tactile–US image feed ($i\mathbb{F}_v$), generates regions of interest (ROIs) around the aligned
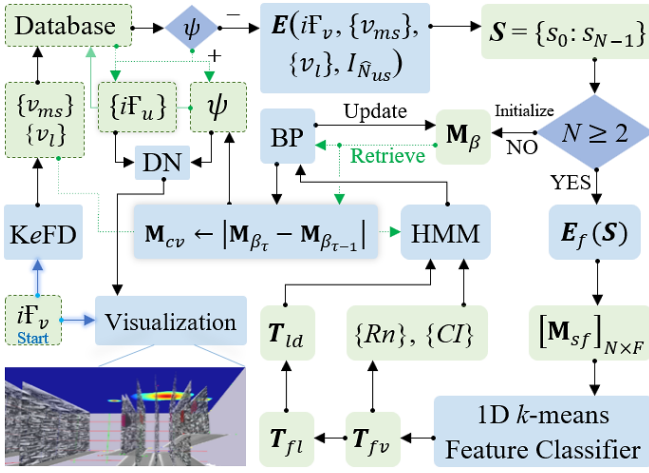
Figure 1. Framework for autonomous detection and image guidance. The green blocks are data, with dashed blocks indicating image data. Blue blocks are functions. Solid green arrows indicate data saved in the database and dotted arrows show data retrieval. Black arrows denote process flow. Notations used: $i\mathbb{F}_v$: tactile–US image feed; **KeFD**: knowledge-encoded feature detector; $\{v_{ms}\}$ and $\{v_l\}$: sets of segmented masks and labels; $i\mathbb{F}_u$: preexisting unclassified feeds; ψ: texture model; **DN**: decision network; $E(\bullet)$: iterative convolution; S: texture sample set; **BP**: belief propagation; $\mathbf{M}_\beta$: belief matrix; $\mathbf{M}_{\beta_\tau}$ and $\mathbf{M}_{\beta_{\tau-1}}$: current and previous belief matrices in time; $\mathbf{M}_{cv}$: convergence matrix; **HMM**: hidden Markov model; $E_f(S)$: feature extractor of set S; $[\mathbf{M}_{sf}]_{N \times F}$: feature matrix of N samples and F features; T_{fv}, T_{fl} and T_{ld}: tensors of feature values, feature labels, and label distributions; $\{Rn\}$ and $\{CI\}$: ranges and confidence intervals of values in T_{fv}.

US regions and passes them through a series of filters. The resulting regions within the ROIs are then labelled as either tumors or nontumors. These labels need to be assessed further.

B. Autonomous Tumor Detection and Guidance Framework

Fig. 1 illustrates the framework for autonomous tumor detection and texture-based image guidance. The sets of segmented masks, $\{v_{ms}\}$, and labels, $\{v_l\}$, of a $i\mathbb{F}_v$ from the **KeFD** are first stored in a **database**. Here, v is the feed serial and v_{ms} and v_l are the associated sets of masks and labels belonging to the US image at v. If the **database** contains a texture model, denoted as ψ_+, the preexisting unclassified feeds in the **database**, $\{i\mathbb{F}_u\}$, are matched to the model ψ and classified in a decision network (**DN**) function. If no unclassified data exists, only the current $i\mathbb{F}_v$ is classified. This completes the autonomous tumor detection workflow. The result is visualized in real-time.

The guidance workflow activates when no texture model is found, denoted as ψ_-. At first, the US v_{ms} of the current $i\mathbb{F}_v$ are consecutively convolved with the current normalized US image $(I_{\hat{N}_{us}})$ to sample the corresponding US texture regions in an iterative convolution routine $E(i\mathbb{F}_v, \{v_{ms}\}, \{v_l\}, I_{\hat{N}_{us}})$. Resulting texture samples are accumulated in a set $S = \{s_0: s_{N-1}\}$, where N denotes the sample quantity. If it is the very first feed $i\mathbb{F}_{v=0}$, a belief matrix $\mathbf{M}_\beta$ is initialized. Here β is the belief ratio. The $\mathbf{M}_\beta$ rows list the GLCM texture features including angular second moment, energy, contrast, homogeneity, inverse difference moment, entropy, and mean. The columns list the beliefs on the sample labels once the sample feature values are clustered. At least two samples ($N \geq 2$) are required to next activate a feature extractor $E_f(S)$. For each texture sample in S, it calculates the GLCM feature vector (v_f) and stores that row-wise in matrix
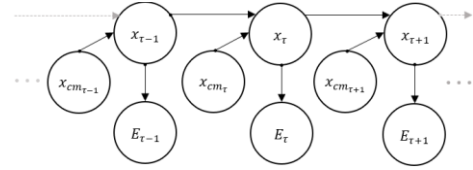

Figure 2. HMM to observe accumulated data in a cl over time. x_τ depends on $x_{\tau-1}$ and x_{cm_τ}. E_τ is the observed evidence at time τ.

$[\mathbf{M}_{sf}]_{N \times F}$. Here, s is the row-wise sample index from 0 to N and f is the column index for each feature value in v_f from 0 to F. Thus, a $\mathbf{M}_{sf}$ column vector contains the values of a feature across the N samples. $\mathbf{M}_{sf}$ is then passed to a **feature classifier**. It applies the **1D k-means** filter with $k = 2$ to each column vector in $\mathbf{M}_{sf}$ to segregate the content into two clusters $cl \in \{0, 1\}$. As a result, the $\mathbf{M}_\beta$ columns are updated as $cl_{0/1}\beta_{t/nt}$, where β_t and β_{nt} denote the beliefs for $t$umor and $n$on$t$umor state labels. The sum of β for a clustered feature value (i.e., $cl_0\beta_t + cl_0\beta_{nt}$) always adds up to 1.0. The clustered column vectors of $\mathbf{M}_{sf}$, denoted now as $cl_{0/1}$, are stored in a tensor T_{fv}. The ranges, $\{Rn\}$, and the confidence intervals, $\{CI\}$, are computed along both cl_0 and cl_1 to define their differences in each feature. In another tensor T_{fl}, the state labels (i.e., t or nt) of the individual values in cl_0 and cl_1 across the features are stored. The state labels are deduced from the v_l of the parent $i\mathbb{F}_v$. The accumulated distribution of these labels in cl_0 and cl_1 across the features are stored in the last tensor T_{ld}. These three tensors allow the $cl_{0/1}$ data to be modeled using an HMM.

C. Modelling Clustered Sequential Data using HMM

Fig. 2 illustrates the HMM that was adopted to represent long- and short-term dependencies among the clustered data. The US textures that the next $i\mathbb{F}_v$ has are unknown. However, clustering the feature values at $i\mathbb{F}_v$ allows the similarity of the next value in a cl to the existing ones to be predicted. As shown, state x_τ of an $i\mathbb{F}_v$ added into a cl at τ depends on the previous state $x_{\tau-1}$ and the hidden state x_{cm_τ} updated at each τ evaluating $(\sum_{i=0 \to \tau} x_i = \langle t \text{ or } nt \rangle)/(\sum_{i=0 \to \tau} \forall x_i)$. It computes the ratio of the total number of a particular state (i.e., t or nt) to the total number of all states accumulated in a cl untill τ. Hence, x_{cm_τ} is the maximum likelihood for an overall state of a cl given long-term observations. Lastly, E_τ is the evidence observed in $i\mathbb{F}_v$ at τ. Three batches ($B_{0:2}$) of x_{cm_τ} distributions were determined empirically to describe state transition probabilities $P(x_\tau | x_{\tau-1})$ based on label accumulations in a cl. Each batch constitutes a different conditional probability matrix $\mathbf{M}_{cp}$, selected based on the updated value of x_{cm_τ}. Likewise, the system performance without image guidance comprises the maximum likelihood estimates of E_τ called the emission probabilities $\varepsilon(E_\tau | x_\tau)$ that constitute the system confidence matrix $\mathbf{M}_{sc}$. These matrices (see the Appendix) model the training operation of the HMM.

D. Belief Propagation (BP)

The proposed HMM is a recurrent Bayesian network that can estimate the belief on x_τ of a cl given states $x_{\tau-1}$ and x_{cm_τ}. When multiple hidden states govern an observed state in HMM, as in our case, the event space can be expressed using the extended form of Bayes' theorem (1),

$$P(A_k | B) = \frac{P(A_k)P(B | A_k)}{\sum_n P(A_n)P(B | A_n)}. \tag{1}$$

TABLE I. RECURSIVE BAYESIAN FILTER FOR BP

for $\forall x_\tau$ in a $cl \in \{0, 1\}$, where $x_\tau \in \{t, nt\}$

$\quad \bar{\beta}(x_\tau) = \sum_{x_{\tau-1}} \beta(x_{\tau-1}) P(x_\tau | x_{\tau-1}, x_{cm_\tau})$

$\quad \beta(x_\tau) = \lambda \bar{\beta}(x_\tau) \varepsilon(E_\tau | x_\tau)$, where $\lambda = \dfrac{1.0}{\sum_{x_\tau \in \{t, nt\}} \bar{\beta}(x_\tau) \varepsilon(E_\tau | x_\tau)}$

end

$\mathbf{M}_{\beta_\tau} \leftarrow \beta(x_\tau)$

Here, $P(A_k|B)$ is the posterior probability of state A_k given the probability of event B. $P(B|A_k)$ is the likelihood estimate of B given A_k while $P(A_k)$ is the prior probability of A_k. $\sum_n P(A_n)P(B|A_n)$ is the summation of all evidential probabilities of all possible states of event A. Therefore, expressing $1/(\sum_n P(A_n)P(B|A_n))$ as a normalizing constant λ, $P(A_k|B)$ can be redefined as the belief of A_k as

$$P(A_k|B) = \lambda P(A_k)P(B|A_k). \quad (2)$$

This is the probability model exercised to update a prior to a posterior belief considering new evidence. As similar labels are accumulated in a cl as more $i\mathrm{F}_v$s are acquired, this belief is expected to gradually increase. To observe this, the recursive Bayesian filter outlined in Table 1 is adopted. There, $\bar{\beta}(x_\tau)$ is the propagated posterior belief governed by $\beta(x_{\tau-1})$, the prior belief, and $P(x_\tau | x_{\tau-1}, x_{cm_\tau})$, the transition probabilities at x_τ. $\beta(x_\tau)$ is the updated belief on x_τ after applying the appropriate $\varepsilon(E_\tau | x_\tau)$ on the observed data from the **KeFD** to the propagated belief $\bar{\beta}(x_\tau)$. $\beta(x_\tau)$ of a current $i\mathrm{F}_v$ is stored in $\mathbf{M}_{\beta_\tau}$ and the changes from the previous $i\mathrm{F}_{v-1}$ are stored as

$$\mathbf{M}_{cv} \leftarrow |\mathbf{M}_{\beta_\tau} - \mathbf{M}_{\beta_{\tau-1}}|, \quad (3)$$

where $\mathbf{M}_{\beta_{\tau-1}}$ is the previous belief matrix and $\mathbf{M}_{cv}$ is the convergence matrix. As $\mathbf{M}_{\beta_{\tau-1}}$ updates to $\mathbf{M}_{\beta_\tau}$, the CI, RN, and $\psi_{t \text{ or } nt}$ for both $cl_{0 \text{ and } 1}$ in each feature also update. When $\mathbf{M}_{cv}$ converges, the acquired states of these components are taken as the learned contents to activate autonomous detection. For $\mathbf{M}_{cv}$ to converge, the argument in (4) must be satisfied for at least one of the column vectors in $\mathbf{M}_{cv}$ that defines the texture types detected in an $i\mathrm{F}_v$.

$$\beta \geq \beta_{Th} \wedge RMSD \begin{pmatrix} \mathbf{M}_{cv} \\ \forall c \in \{0:3\} \end{pmatrix} \leq \xi \wedge \mu \begin{pmatrix} \mathbf{M}_{\beta_\tau} \\ \forall c \in \{0:3\} \end{pmatrix} \geq \mu \begin{pmatrix} \mathbf{M}_{\beta_{\tau-1}} \\ \forall c \in \{0:3\} \end{pmatrix} \quad (4)$$

The belief β must reach a threshold β_{Th}. The *r*oot *m*ean *s*quared *d*ifference (RMSD) along a $\mathbf{M}_{cv}$ column should be negligibly small to indicate saturation. And, the mean belief on a cl state at τ must be greater or equal to that at $\tau - 1$. For the results presented in this paper, $\beta_{Th} = 0.8$ and $\xi = 0.05$ were used.

III. EXPERIMENTS AND RESULTS

Acquiring a significant number of deflated animal lungs was not feasible as it required clinically induced atelectasis. 20 *ex vivo* porcine liver specimens were injected with liquid agar to simulate deflated lung tumors [18]. All specimens were imaged with C-arm fluoroscopy imaging (OEC 9900 elite, General Electric, Fairfield, CT, USA) to attain preoperative images. Each specimen was palpated three times in a staged MIS (Fig. 3a) with and without texture-based guidance, amounting to a total of 120 conducted trials to produce a database of 1784 pairs of tactile–US images. An expert operator conducted all of the trials, as it was important to maintain consistent imaging quality
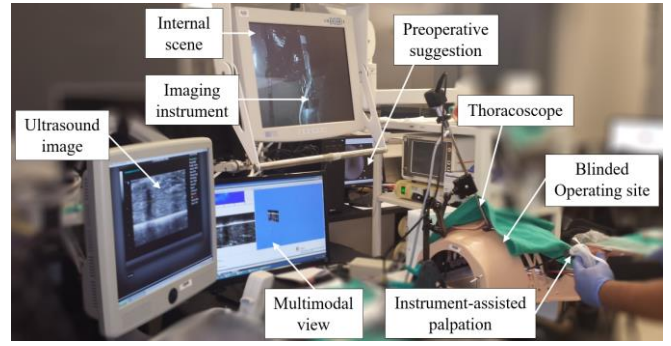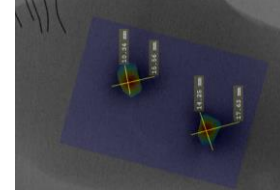

Figure 3. (a) The MIS experimental setup.

Figure 3. (b) Fused palpation map registered to fluoroscopy images.
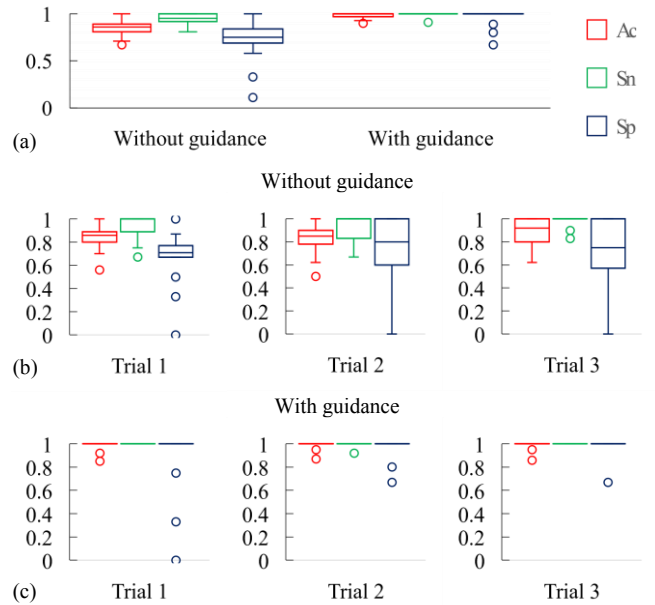

Figure 4. (a) Comparing localization accuracies with and without guidance. (b) Accuracies observed in each trial without guidance. (c) Difference observed after adding texture-based guidance for palpation in MIS.

to validate the proposed work. A multiple participant-based study could not be designed as a lack of experience and skill in maneuvering the multisensory imaging device in MIS generated large variabilities in the quality of the datasets. Nevertheless, to remove sources of bias, an assistant was recruited to deliver deidentified random specimens and their fluoroscopy images to the MIS site one at a time and to keep track of the completed trials on each specimen. In every trial, the guided and the non-guided palpations were conducted alternatively. Accuracy (Ac), sensitivity (Sn) and specificity (Sp) were evaluated for each labelled tactile–US image in each captured sequence using (5).

$$Ac = \frac{\mathrm{T}_t + \mathrm{T}_{nt}}{\mathrm{T}_t + \mathrm{T}_{nt} + \mathrm{F}_t + \mathrm{F}_{nt}}; Sn = \frac{\mathrm{T}_t}{\mathrm{T}_t + \mathrm{F}_{nt}}; Sp = \frac{\mathrm{T}_{nt}}{\mathrm{T}_{nt} + \mathrm{F}_t} \quad (5)$$

Here, T_t and T_{nt} are the number of true tumors and nontumors identified, while F_t and F_{nt} are the number of false
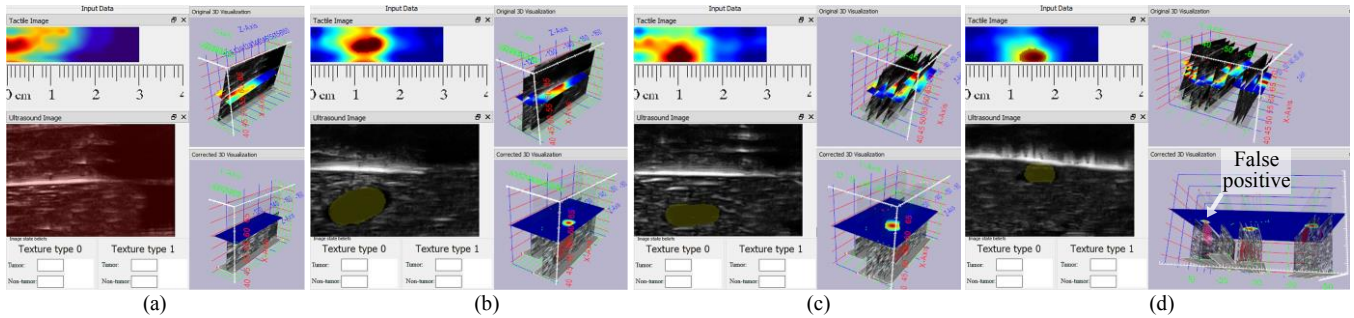
Figure 5. **KeFD** classifier results without texture-based guidance in MIS. (a) Correct detection of nontumor region. (b) and (c) Correct subsequent detections of tumor regions. (d) Detection of false positives, as labelled, in addition to correct tumor detections.
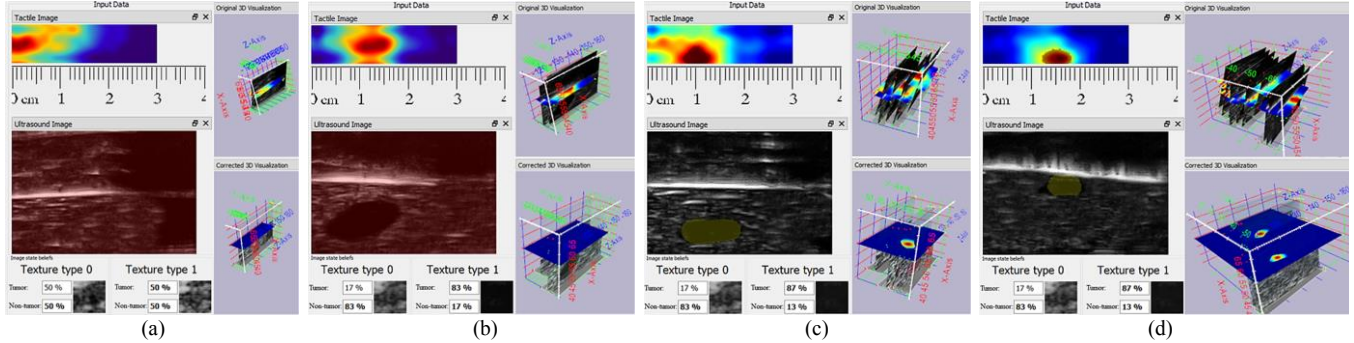

Figure 6. Texture-guided palpation imaging in MIS. (a) and (b) Updating beliefs on detected texture types. (c) Retrospective localization once beliefs converge. (d) Autonomous detection of a tumor texture region in a future image.

TABLE II. COMPARING TEXTURE-GUIDED TC–US IMAGING TO PREVIOUS SYSTEMS AND OTHER SYSTEMS IN LITERATURE

Methods	Specimen	Ac	Sn	Sp
Robotics-assisted TSI [20]	*ex vivo* bovine liver	0.82	0.89	0.62
TSS [18]	*ex vivo* bovine liver	0.67	0.83	0.33
US [18]	*ex vivo* bovine liver	0.58	0.67	0.42
SWE-US with DPN [21]	Breast tumors	0.95	0.98	0.94
US-USE with CNN [22]	Thyroid nodules	0.94	0.92	0.97
TC–US w/o guidance	*ex vivo* porcine liver	0.85	0.95	0.73
TC–US with guidance	*ex vivo* porcine liver	0.98	0.99	0.97

tumors and nontumors indicated. To cross-validate the tumor detections, the fused localization maps were scaled and overlaid on the fluoroscopy images (Fig. 3b). The smallest tumor the system could detect was 2 *cm* [19]. Fig. 4a compares the mean localization accuracies with and without the guidance across the image sequences acquired. With guidance, Ac improved from 85% to 98%, Sn from 95% to 99% and most notably Sp from 73% to 97%. This indicates that the system could classify texture samples based on their feature characteristics even if the source images were partially mislabeled by **KeFD**. Fig. 4b compares the trials without guidance. Both Ac and Sn improved over time, likely due to better palpation resulting from experience and skill acquisition; however, the large interquartile ranges in trials 2 and 3 for Sp indicate the limitation of the **KeFD**. With guidance activated, the difference is clear in all trials shown in Fig. 4c. This time, Sp also had some outliers in trials 1 and 2 that were reduced by trial 3.

IV. DISCUSSIONS AND CONCLUSIONS

Table II compares the results of this work to other published results. The tactile–US guidance results are better than that of the robotics-assisted TSI (tactile sensing instrument) [20]. Given

a force and a position-controlled model, it could objectively detect the tumor sites accurately. However, the lower Sp shows that it could not detect the nontumor sites as well. That is because the visual representation of the force applied on the tissue sometimes resulted in false positives and false negatives. With the handheld TSS (tactile sensing system) [18] or the US probe [18], tumor detection relied entirely on human interpretation of the visualizations. The results were poorer since the readings could not be objectively analyzed at the time. With tactile–US imaging, real-time analysis became possible through the **KeFD**. This led to better results, as depicted in Fig. 5. It could accurately detect both the tumor and the nontumor sites (Fig. 5a–c) automatically, but it also detected false positives at times (Fig. 5d). Ac and Sp were lower since palpation could not be done in a directed manner. With the addition of guidance, the results improved significantly. Fig. 6 demonstrates how the system directs texture-guided palpation imaging in MIS. At the start, no labelled texture is available. As images are acquired, note the detected textures and the updating beliefs on their types in Fig. 6a–b, belief convergence availing retrospective detection in Fig. 6c, and automated detection onward in Fig. 6d. Note that with learned texture incorporated, the false positive from Fig. 5d is also eliminated in Fig. 6d. The results are now similar to some of the clinically-tested highly accurate AI systems [21, 22]. This holds promise that the proposed method will perform well when tested in *in vivo* models.

In this paper, a texture-based guidance method for palpation imaging-based tumor localization in MIS was introduced. The results demonstrate a significant improvement over previous work. Tumor localization effort was minimized through directed palpation, compared to strenuous palpation needed without guidance. Future work will focus on further improvement and validation on deflated lung specimens and *in vivo* models.

APPENDIX

EMPIRICALLY DETERMINED TRANSITION AND EMISSION PROBABILITIES

(a) Conditional probability matrix $\mathbf{M}_{cp}$

			x_τ	
	states			
	x_{cm_τ}	$x_{\tau-1}$	t	nt
$\mathbf{B_0}$:	$(x_{0\to\tau} = t)\% \geq 0.6$	t	0.9	0.1
	$(x_{0\to\tau} = nt)\% < 0.6$	nt	0.8	0.2
$\mathbf{B_1}$:	$(x_{0\to\tau} = t)\% = 0.5$	t	0.5	0.5
	$(x_{0\to\tau} = nt)\% = 0.5$	nt	0.5	0.5
$\mathbf{B_2}$:	$(x_{0\to\tau} = nt)\% \geq 0.6$	t	0.2	0.8
	$(x_{0\to\tau} = t)\% < 0.6$	nt	0.3	0.7

(b) System confidence matrix $\mathbf{M}_{sc}$

		E_τ	
	states	t	nt
x_τ	t	0.95	0.05
	nt	0.27	0.73

REFERENCES

[1] Canadian Cancer Society, "Treatments for non-small cell lung cancer," *cancer.ca*, [Online]. Available: http://www.cancer.ca/en/cancer-informati on/cancer-type/lung/treatment/?region=on. [Accessed: Jan. 10, 2018].

[2] A. Teatini *et al.*, "The effect of intraoperative imaging on surgical navigation for laparoscopic liver resection surgery," in *Nature Scientific Reports*, vol. 9, no. 18687, pp. open access, Dec. 2019.

[3] T. Langø, T. Hernes and R. Mårvik, "Navigated ultrasound in laparoscopic surgery," in *Advances in Laparoscopic Surgery*, A. Malik, Ed. Rijeka, Croatia: InTech, 2012, pp. 77–98.

[4] A. Miller, "Practical approach to lung ultrasound," *BJA Education*, vol. 16, no. 2, pp. 39–45, 2016.

[5] C. Huang, Q. Wang, *et al.*, "Tactile perception technologies and their applications in minimally invasive surgery: a review," in *Frontiers in Physiology*, vol. 11, pp. open access, Dec. 2020.

[6] D. Avivi, "A novel minimally invasive tumor localization device," M.E.Sc. thesis, Biomed. Eng., Western University, London, ON, Canada, 2016.

[7] A. S. Naidu, M. D. Naish and R. V. Patel, "A breakthrough in tumor localization: combining tactile sensing and ultrasound," in *IEEE Robotics & Automation Magazine*, vol. 24, no. 2, pp. 54–62, 2017.

[8] A. Escoto *et al.*, "A multi-sensory mechatronic device for localizing tumors in minimally invasive interventions," *IEEE Int Conf on Rob and Autom (ICRA)*, Seattle, WA, USA, 2015, pp. 4742–4747.

[9] A. Shamsil *et al.*, "A computational model for estimating tumor margins in complementary tactile and 3D ultrasound images," in *Proc. of SPIE Medical Imaging*, vol. 9786, San Diego, CA, USA, 2016.

[10] F. Davnall *et al.*, "Assessment of tumor heterogeneity: an emerging imaging tool for clinical practice?," *Insights into Imaging*, vol. 3, no. 6, pp. 573–589, 2012.

[11] I. Phillips *et al.*, "Clinical applications of textural analysis in non-small cell lung cancer." *The Brit Jrnl of Rad*, vol. 91, no. 1081, p. 20170267, 2018.

[12] P. Nguyen *et al.*, "Grey scale texture analysis of endobronchial ultrasound mini probe images for prediction of benign or malignant aetiology," *Respirology*, vol. 20, no. 6, pp. 960–966, 2015.

[13] S. Veeramani and E. Muthusamy, "Detection of abnormalities in ultrasound lung image using multi-level RVM classification," *The J of Mat-Fet & Neon Med*, vol. 29, no. 11, pp. 1844–1852, 2015.

[14] L. Nahlawi *et al.*, "Stochastic Modeling of Temporal Enhanced Ultrasound: Impact of Temporal Properties on Prostate Cancer Characterization," *IEEE TBME*, vol. 65, no. 8, pp. 1798–1809, 2018.

[15] W.-L. Du, Y. Zhou, J. Zhao and X. Tian, "K-means clustering guided generative adversarial networks for SAR-optical image matching," in *IEEE Access*, vol. 8, pp. 217554–217572, 2020.

[16] W. Gomez *et al.*, "Analysis of co-occurrence texture statistics as a function of gray-level quantization for classifying breast ultrasound," *IEEE TMI*, vol. 31, no. 10, pp. 1889–1899, Oct. 2012.

[17] A. R. Mesquita, "Parsimonious Bayesian filtering in Markov jump systems with applications to networked control," *IEEE Transactions on Automatic Control*, vol. 66, no. 1, pp. 76–88, Jan. 2021.

[18] M. T. Perri *et al.*, "New tactile sensing system for minimally invasive surgical tumor localization," *Int J Med Robotics Comput Assist Surg*, vol. 6, pp. 211–220, 2010.

[19] Canadian Cancer Society, "Stages of non-small cell lung cancer," cancer.ca, [Online]. Available: https://www.cancer.ca/en/cancer-informati on/cancer-type/lung/staging/?region=on, [Accessed: Apr 25, 2021].

[20] A. Talasaz and R. V. Patel, "Integration of force reflection with tactile sensing for minimally invasive robotics-assisted tumor localization," in *IEEE Tran. on Haptics*, vol. 6, no. 2, pp. 217–228, 2013.

[21] Q. Zhang *et al.*, "Dual-mode artificially-intelligent diagnosis of breast tumors in shear-wave elastography and B-mode ultrasound using deep polynomial networks," *Med Eng & Phys*, vol. 64, pp. 1–6, 2019.

[22] P. Qin, *et al.*, "Diagnosis of benign and malignant thyroid nodules using combined conventional ultrasound and ultrasound elasticity imaging," *IEEE J of Biom and Health Inform*, vol. 24, no. 4, pp. 1028–1036, 2020.